

Silicon Photonic Structures: Mach-Zehnder Interferometers and Ring Resonators.

Anthony Tkalec, anthony.tkalec@mail.mcgill.ca
edX UBCx Phot1x course, course username Anttk97

Abstract – The Mach-Zehnder Interferometer (MZI) and optical ring resonator are fundamental optical devices widely used in silicon photonic applications, including optical sensing, phase measurement, and optoelectronic modulation. This study explores various implementations of imbalanced MZIs with targeted Free Spectral Range (FSR) values and the fabrication of matched interferometers to evaluate real-world manufacturing results. In parallel, sixteen variants of add-drop ring resonators were designed, fabricated, and analyzed, with radii ranging from 20 μm to 50 μm and coupling gaps from 140 nm to 200 nm. These structures were studied to determine the effect of the ring radius on FSR and of gap size on the quality factor (Q-factor). Theoretical models were developed to support the analysis, enabling extraction of group indices and prediction of spectral behavior.

I. INTRODUCTION

THE Mach-Zehnder Interferometer (MZI) and optical ring resonator are fundamental components in silicon photonics. MZIs are widely used in applications such as phase sensing, optical filtering, and modulation. By leveraging constructive and destructive interference between two optical paths of differing lengths, they allow for precise spectral control. Their high sensitivity to refractive index changes also makes them suitable for sensing applications, including biosensing. This work investigates four MZI configurations—one balanced and three imbalanced—designed to achieve target Free Spectral Range (FSR) values of 3 nm, 5 nm, and 10 nm.

Complementing the MZIs, this study also explores optical ring resonators—compact, wavelength-selective devices where light is coupled into a looped waveguide and interacts resonantly. Like MZIs, ring resonators are highly sensitive to environmental changes and are well-suited for sensing and filtering applications [1]. Sixteen variants of add-drop ring resonators were designed, simulated, fabricated and characterized, with radii varying from 20 μm to 50 μm in 10 μm steps, and coupling gaps from 140 nm to 200 nm. The variations in these designs allow for the evaluation of how the ring radius affects the FSR, and how the coupling gap influences resonance depth and quality factor (Q-factor).

II. THEORY

To begin with the MZI, consider a Y-branch splitter,

consisting of single mode waveguides, disregarding the field distribution within the waveguides. Given light as input to the splitter with an input intensity of I_i and with an electric field E_i , it is split with a 50:50 ratio. The first output of the Y-branch then consists of the power output intensity of $I_1 = \frac{I_i}{2}$ and field $E_1 = \frac{E_i}{\sqrt{2}}$, similarly for the second output $I_2 = \frac{I_i}{2}$ and field $E_2 = \frac{E_i}{\sqrt{2}}$. The propagation of the light through both waveguides can be expressed with the following equations $\beta_1 = \frac{2\pi n_1}{\lambda}$ and $\beta_2 = \frac{2\pi n_2}{\lambda}$ respectively. With lengths L_1 and L_2 and disregarding any propagation losses, the output fields can be described with:

$$\begin{aligned} E_{o1} &= E_1 e^{-i\beta_1 L_1} \\ E_{o2} &= E_2 e^{-i\beta_2 L_2} \end{aligned}$$

Combined at the second Y-branch, the output field is then as follows:

$$E_o = \frac{E_{o1} + E_{o2}}{\sqrt{2}}$$

The intensity at the combined output is now:

$$I_o = \frac{I_i}{4} \left[2 \cos \left(\frac{\beta_1 L_1 - \beta_2 L_2}{2} \right) \right]^2$$

Eventually simplified to the following transfer function:

$$\frac{I_o}{I_i} = \frac{1}{2} [1 + \cos(\beta_1 L_1 - \beta_2 L_2)]$$

For an imbalanced MZI, the FSR can be determined as follows, with $\Delta L = \text{abs}(L_2 - L_1)$.

$$FSR[m] = \frac{\lambda^2}{n_g \Delta L}$$

As ΔL nears 0, the FSR of the MZI will approach infinity. The first design to be evaluated consists of a designed ΔL of 0.

With respect to ring resonators, one key concept is of the resonance, the resonance occurs at the exact wavelength where there is constructive interference. This depends on the total round-trip length of the ring L_{rt} . In the simple case consisting of a circular ring, $L_{rt} = 2\pi R$. Resonance can then be seen at integer multiples M in 2π intervals.

$$\text{round trip phase} = \frac{2\pi n_{\text{eff}}}{\lambda} L_{rt} = M2\pi$$

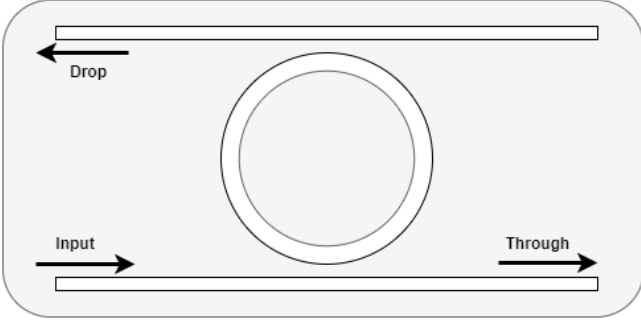


Figure 1 – Add-drop ring resonator structure

Figure 1 illustrates the basic structure of the double bus add-drop ring resonator which is the configuration to be examined further in this report. The ring radius is to be varied which will affect the length L_{rt} , directly impacting the FSR given the following:

$$FSR = \frac{\lambda^2}{L_{rt} n_g}$$

The Q-factor quantifies how sharply the resonance frequency (ν) is selected. It is defined as the ratio of the resonant frequency to the resonance linewidth ($\Delta\nu_{\frac{1}{2}}$):

$$Q = \frac{\nu}{\Delta\nu_{\frac{1}{2}}}$$

If adjusting the gap from the ring to the nearby waveguides, we can control the loss (A) which impacts the Q factor, as a function of loss and field transmission coefficients of the couplers (t_1, t_2), the field self-coupling coefficient t is related to the coupling coefficient as per the following $t = \sqrt{1 - |\kappa|^2}$ [2]. The expression for the loaded quality factor is then:

$$Q = \frac{\pi \sqrt{A t_1 t_2}}{1 - A t_1 t_2} \cdot \frac{\lambda}{\Delta\lambda}$$

As described, reducing the gap increases coupling due to a larger $|\kappa|^2$, which decreases the field transmission coefficients t_1, t_2 , thereby lowering the Q-factor due to increased power loss into the bus waveguides.

III. MODELLING AND SIMULATION

Using *Lumerical MODE FDE*, a 500 nm width by 220 nm height TE polarized Si waveguide has been modelled. This is the chosen specification for the waveguides in both the MZIs and ring resonators to be fabricated and evaluated in later sections. The electric field intensity for the TE mode is illustrated in Figure 2.

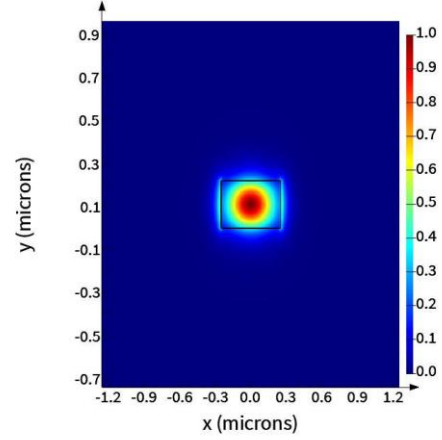


Figure 2 - TE mode profile

The TM mode, while not planned to be further analyzed, has been simulated and is illustrated in Figure 3.

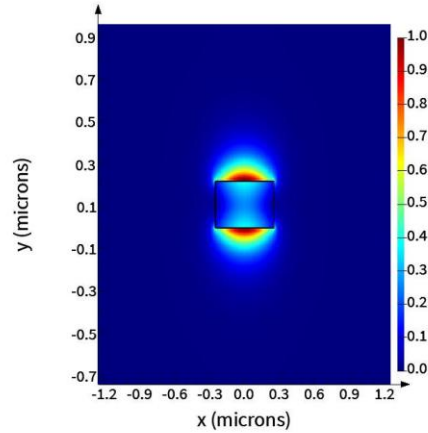


Figure 3 - TM mode profile

Simulating the effective index resulted in Figure 4, the real part (blue) and imaginary part (green) of the effective index are illustrated.

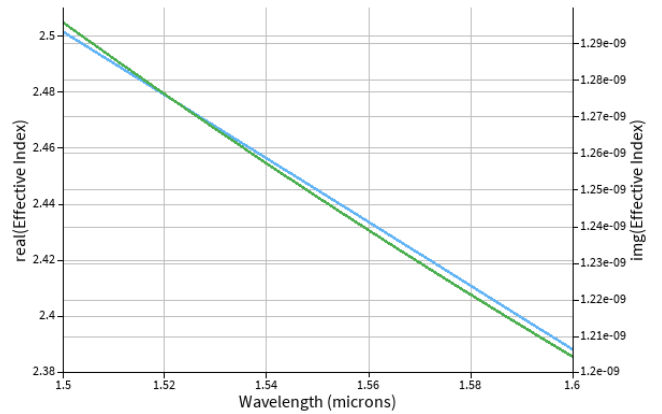


Figure 4 - Effective index

The group index from 1500 nm to 1600 nm is illustrated in Figure 5.

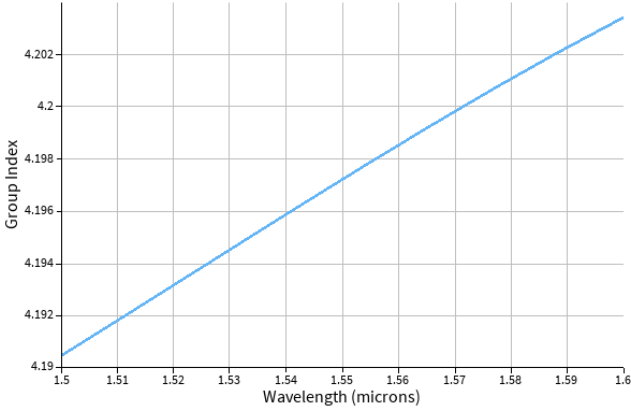


Figure 5 - Group index

With *Lumerical MODE FDE*, the following compact model was obtained for the waveguide.

$$n_{eff}(\lambda) = 2.44 - 1.33(\lambda - \lambda_0) - 0.042(\lambda - \lambda_0)^2$$

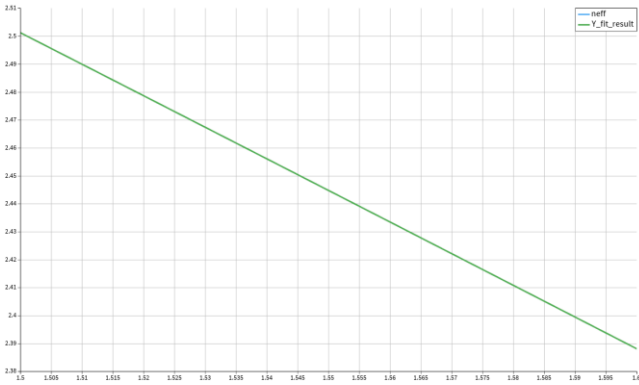


Figure 6 - Compact model fit

There are four designs to be evaluated, and five circuits. Two equivalent matched interferometers for the purpose of evaluating the real world, measured differences in manufacturing between identical designs. This may prove helpful in justifying any possible discrepancies between any of the following simulations and real results. Figure 7 illustrates the expected results from the balanced interferometers. As can be observed this also appears to be the expected spectrum from a grating coupler.

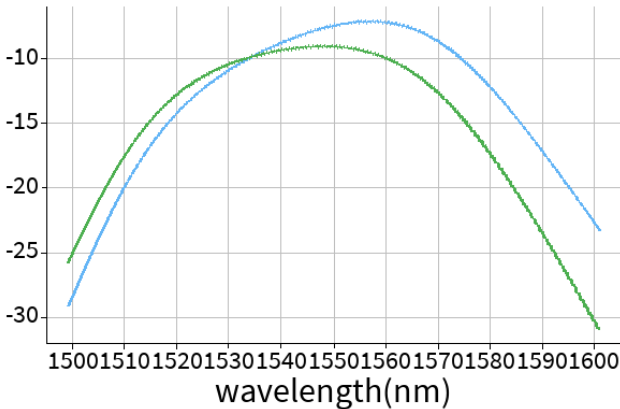


Figure 7 - Balanced interferometer spectrum

Along with the two balanced MZI designs, three more have been designed based on varying FSR values.

Table 1 – Chosen FSR and ΔL values

FSR	ΔL
3 nm	191.11 μm
5 nm	111.46 μm
10 nm	57.34 μm

A simulated spectrum spanning approximately 10 nm for the 3nm FSR variant, with $\Delta L = 191.11 \mu\text{m}$ MZI can be seen in Figure 8.

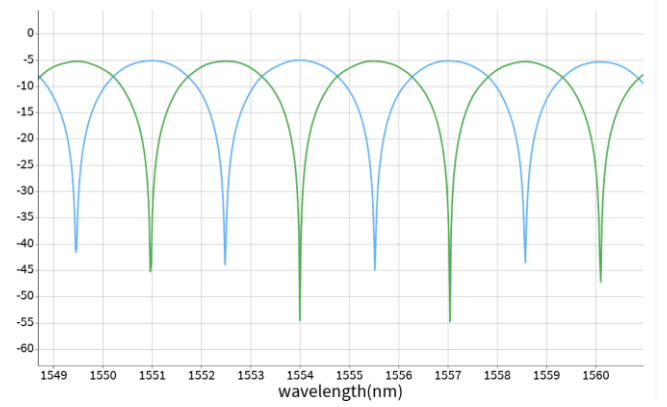


Figure 8 - Spectrum with $\Delta L = 191.11 \mu\text{m}$ and FSR = 3 nm

Figure 9 is a screenshot from *KLayout*, showing the structures of the discussed interferometers. The two leftmost MZIs are duplicate balanced interferometers, and the remaining are of the 3nm, 5nm and 10nm FSR versions. The imbalanced interferometers path length differences have been designed to exactly match the ΔL as specified in Table 1.

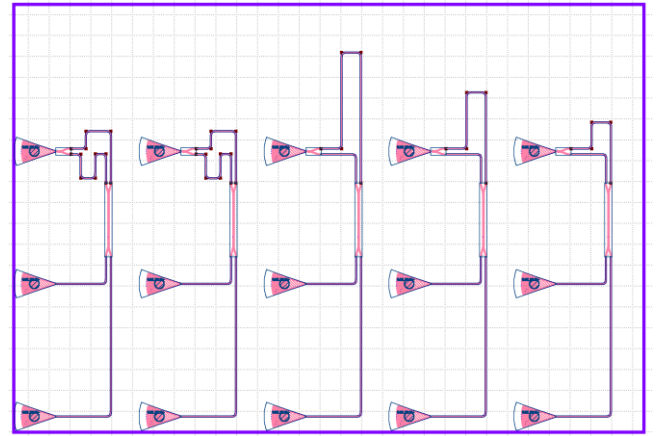


Figure 9 - MZI structures as designed in *KLayout*

There are sixteen optical ring resonators which have been designed and simulated, the variations in design have been made to the ring radius, which is expected to directly affect the FSR (and the Q-factor), as well as the gap between the ring and the waveguide buses. Using a MATLAB script, the designs have all been simulated to have the following expected FSR and Q-factors as described in Table 2, these two parameters are the primary comparison points for the fabricated devices.

Figures 10 and 11 illustrate the data as seen in Table 2, it can be observed that FSR is only expected to be affected by the ring radius, while Q-factor is affected by both the radius and gap.

Table 2 – Optical Ring Resonator Simulation results

Radius(μm)	Gap(nm)	FSR(nm)	Q-factor
20	140	4.883	6844
20	160	4.883	12573
20	180	4.883	20955
20	200	4.883	34286
30	140	3.258	9788
30	160	3.258	17278
30	180	3.258	27271
30	200	3.258	41154
40	140	2.445	12447
40	160	2.445	21254
40	180	2.445	32110
40	200	2.445	45735
50	140	1.954	14884
50	160	1.954	24659
50	180	1.954	35936
50	200	1.954	49004

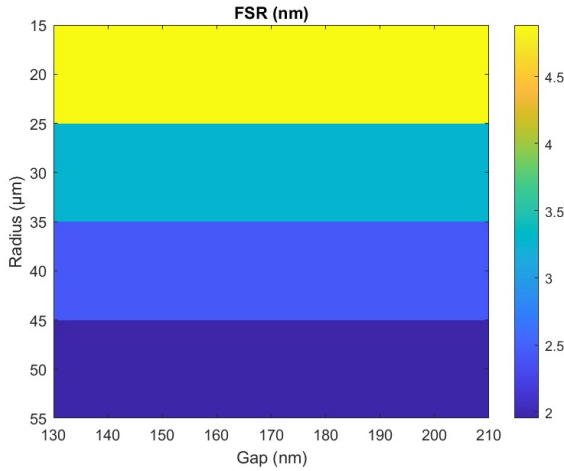


Figure 10 – FSR based on Radius and Gap

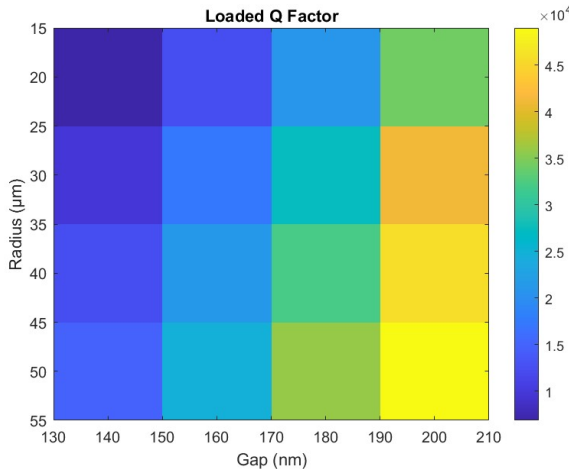


Figure 11 – Loaded Q-factor based on Radius and Gap

Figure 12 depicts a simulation done in *Lumerical* for the ring resonator consisting of a 20 μm radius, and 140 nm gap. The FSR is in line with expectations from Table 2. All have been simulated and are in line with expectations; to remain concise not all have been illustrated in this report.

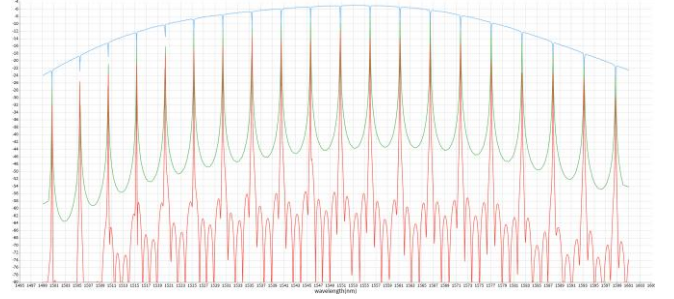


Figure 12 – Lumerical simulation spectrum for ring resonator with radius 20 μm and gap 140 nm

The layout for the ring resonator designs was also completed in *KLayout*. Four separate files consisting of four variants per file were sent for fabrication. Figure 13 below illustrates one of these layouts for reference.

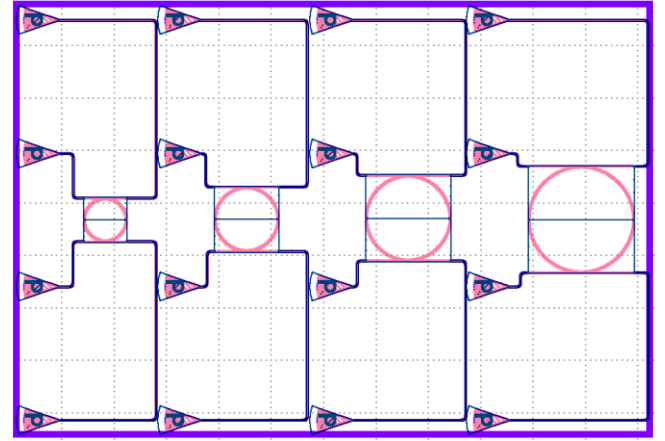


Figure 13 – Ring Resonator structures as designed in KLayout

IV. FABRICATION

Fabrication of these designs was completed on a shared chip by Applied Nanotools, Inc.'s NanoSOI process in Edmonton, Canada. The process is based on direct-write 100 keV electron beam lithography technology. Silicon-on-insulator wafers of 200 mm diameter, 220 nm device thickness and 2 μm buffer oxide thickness are used as the base material for the fabrication. The wafer was pre-diced into square substrates with dimensions of 25x25 mm, and lines were scribed into the substrate backsides to facilitate easy separation into smaller chips once fabrication was complete. After an initial wafer clean using piranha solution (3:1 H_2SO_4 : H_2O_2) for 15 minutes and water/IPA rinse, hydrogen silsesquioxane (HSQ) resist was spin-coated onto the substrate and heated to evaporate the solvent. The photonic devices were patterned using a JEOL JBX-8100FS electron beam instrument at The University of British Columbia. The exposure dosage of the design was corrected for proximity effects that result from the backscatter of electrons from exposure of nearby features. Shape writing order was optimized for efficient patterning and minimal beam drift. After the e-beam exposure and

subsequent development with a tetramethylammonium sulfate (TMAH) solution, the devices were inspected optically for residues and/or defects. The chips were then mounted on a 4" handle wafer and underwent an anisotropic ICP-RIE etch process using chlorine after qualification of the etch rate. The resist was removed from the surface of the devices using a 10:1 buffer oxide wet etch, and the devices were inspected using a scanning electron microscope (SEM) to verify patterning and etch quality. A 2.2 μm oxide cladding was deposited using a plasma-enhanced chemical vapour deposition (PECVD) process based on tetraethyl orthosilicate (TEOS) at 300°C. Reflectometry measurements were performed throughout the process to verify the device layer, buffer oxide and cladding thicknesses before delivery.

Upon completion of fabrication, to then characterize the devices, a custom-built automated test setup [2, 6] with automated control software written in Python was used [3]. An Agilent 81600B tunable laser was used as the input source and Agilent 81635A optical power sensors as the output detectors. The wavelength was swept from 1500 to 1600 nm in 10 pm steps. A polarization maintaining (PM) fibre was used to maintain the polarization state of the light, to couple the TE polarization into the grating couplers [4]. A 90° rotation was used to inject light into the TM grating couplers [4]. A polarization maintaining fibre array was used to couple light in/out of the chip [5].

Throughout any fabrication process there will be variability in the physical outcome when compared to the designed specifications, in this case all waveguides had been designed to be 500 nm in width by 220 nm height. A corner analysis was performed to determine the potential real range the design may fall in, and in turn the range of group indexes that can be expected. The estimated range for the width is between 470 nm and 520 nm, and the height from 193 nm to 224 nm. The designed value has been placed in the below figure for reference.

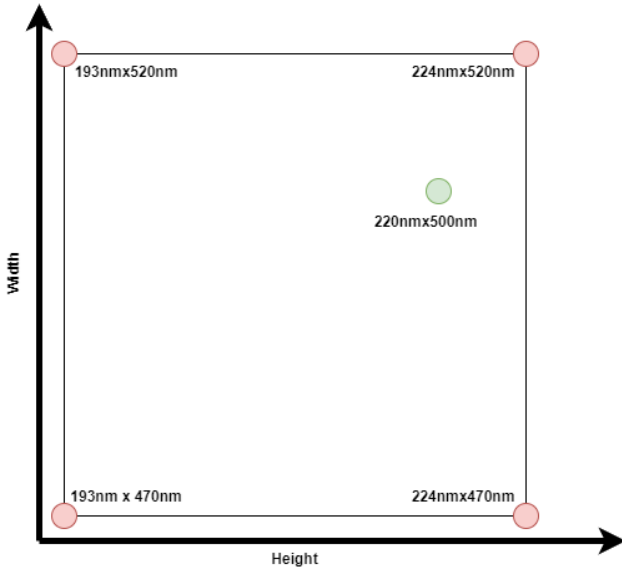


Figure 14 – Corner Analysis visualized

Based on the estimated manufacturing ranges, the waveguide has been re-simulated and the expectation for the group index of the manufactured device is $4.155 < n_g < 4.2$. A perfect value exactly representing the designed waveguide would be if $n_g = 4.19$.

V. EXPERIMENTAL DATA AND ANALYSIS

The collected data spans from 1500 nm to 1580 nm, was collected at 25 degrees C and in the TE mode. This applies to all results and analyses to follow.

Beginning with the MZI data and analysis, five structures were evaluated—four unique designs and one repeated structure for comparison.

For the repeated structure (balanced interferometers), Figure 15 displays the individual responses of both fabricated devices and their averaged spectrum. The observed spectral shape matches expectations for a balanced interferometer.

Figure 16 shows the amplitude difference between the two interferometers for Channels 1 and 2. Across the wavelength range of 1530 nm to 1580 nm, the deviation remains within approximately ± 1 dB. Such variation is likely due to minor experimental fluctuations such as different coupling losses, it is assumed that polarization was equivalent for both measurement results.

Overall, this result demonstrates good measurement repeatability, providing strong evidence that the fabrication process reliably reproduces the designed optical response and that the structures are repeatable as designed.

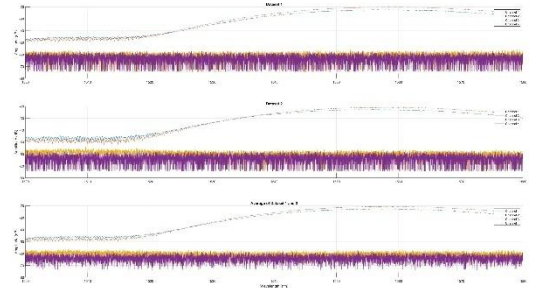


Figure 15 – Balanced interferometer experimental data

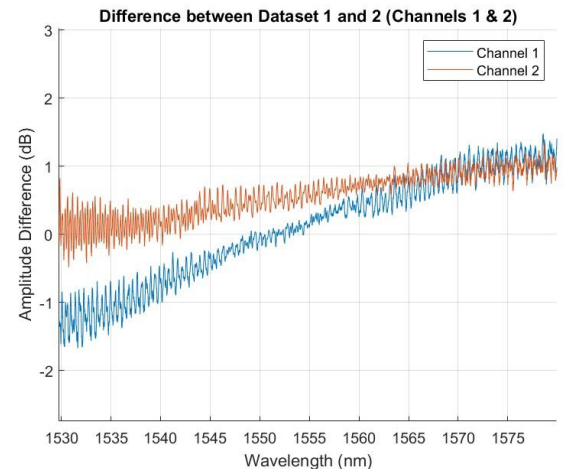


Figure 16 – Difference between both balanced interferometers

For the first imbalanced MZI, given a ΔL of 191.11 μm , the expectation is to have an FSR of 3 nm, with the collected data we can also determine the group index and confirm it falls within the expected $4.155 < n_g < 4.2$. The data has been processed using a modified version of the provided MATLAB code which uses autocorrelation to fit a curve over the experimental data, the fitted curve is shown in red with experimental results in blue.

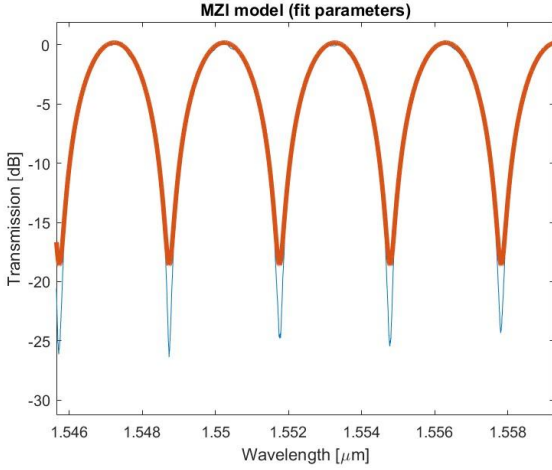


Figure 17 – Experimental data for MZI with $\Delta L = 191.11 \mu\text{m}$

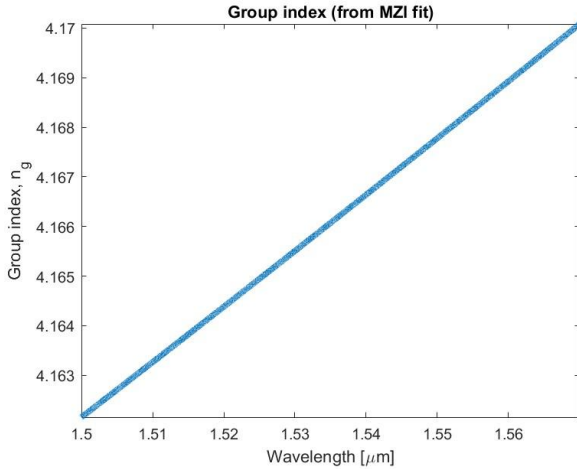


Figure 18 – Experimental data for MZI with $\Delta L = 191.11 \mu\text{m}$, n_g value

The FSR based on the fit curve over the experimental data is 3nm, this is the expected result for this MZI. The group index, n_g is lower than the expected value at 4.16, it does fall in the range of the corner analysis from earlier and is 0.716% off from expectation.

The second MZI, with a ΔL of 111.46 μm , measured an FSR of 5.015nm, 0.3% off expectations.

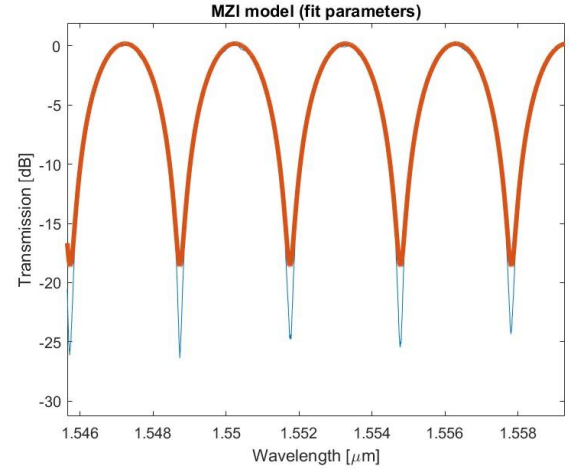


Figure 19 – Experimental data for MZI with $\Delta L = 111.46 \mu\text{m}$

The last MZI with a path length difference of 57.34 μm measured an FSR of 10.02 at 1550 nm, with the result illustrated in Figure 20, this was 0.2% off expectations.

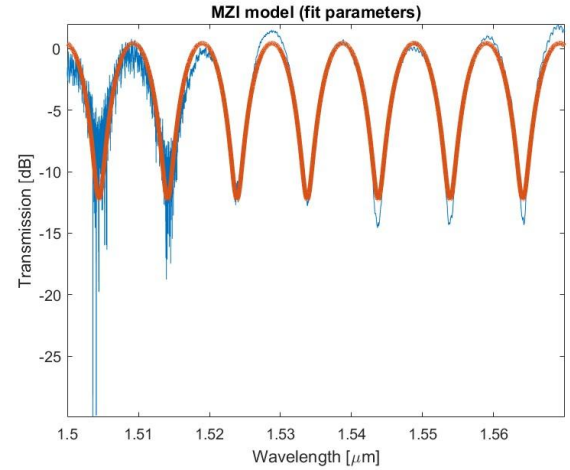


Figure 20 – Experimental data for MZI with $\Delta L = 57.34 \mu\text{m}$.

Regarding the MZIs tested, they all performed well within expectations with the FSR differing by at most 0.3% from the intended design. Table 3 below tabulates these results.

Table 3 – MZI expected to measured FSR results			
MZI ΔL	FSR(expected)	FSR (measured)	Error
191.11 μm	3 nm	3 nm	0%
111.46 μm	5 nm	5.015 nm	0.3%
57.34 μm	10 nm	10.02 nm	0.2%

Analyzing the data collected from the ring resonators, there were two results which were unusable. The data collected is entirely noise for these two results, all power readings below - 50 dBm and no resonance peaks could be observed. The ring resonators with the following radius and gap to be omitted are listed in the table below.

Table 4 – Omitted ring resonator measurements	
Radius	Gap
20 μm	180 nm
20 μm	200 nm

For the remaining fourteen ring resonator measurements, a script was developed in MATLAB to compute both the FSR and Q-factor for each data file. The FSR is determined by the distance from each detected peak in the data, and the q-factor estimated by the resonance wavelength, or position of the peak divided by the full width at half maximum (FWHM) of this peak. Figure 20 illustrates the MATLAB result for the first ring resonator with a 20 μm radius and 140 nm gap. The remaining results will be described in Table 5 as to remain concise.

The FSR and estimated Q-factor is printed in the MATLAB console along with the plot as shown in Figure 21 for a basic validation check that the correct peaks have been detected.

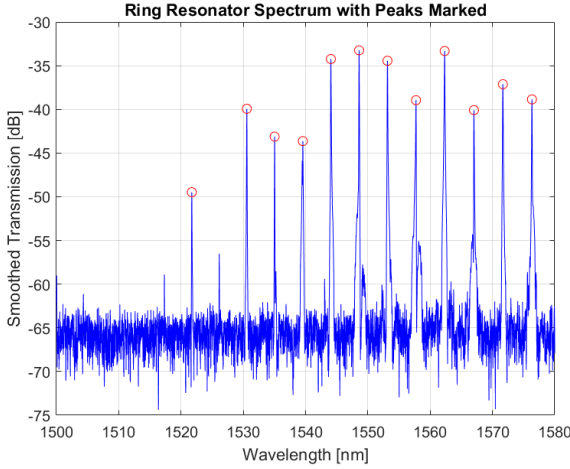


Figure 21 – Processed experimental data for ring resonator

The estimated FSR and Q-factor for this ring resonator are 4.965 nm and 5814 respectively.

Table 5 – Optical Ring Resonator Simulation vs Experimental results

R(μm)	G(nm)	FSR (nm) Expected	Q-factor Expected	FSR (nm) Measured	Q-factor Measured
20	140	4.883	6844	4.965	5814
20	160	4.883	12573	4.559	9203
20	180	4.883	20955	NA	NA
20	200	4.883	34286	NA	NA
30	140	3.258	9788	3.238	4677
30	160	3.258	17278	3.05	7796
30	180	3.258	27271	3.051	9507
30	200	3.258	41154	3.049	13613
40	140	2.445	12447	2.377	5935
40	160	2.445	21254	2.579	8215
40	180	2.445	32110	2.284	10003
40	200	2.445	45735	2.331	11985
50	140	1.954	14884	1.832	5820
50	160	1.954	24659	1.834	7323
50	180	1.954	35936	1.894	10395
50	200	1.954	49004	1.899	13347

The measured results follow expected trends but do not quite match up perfectly, the largest deviation in FSR from expected results is for the ring resonator with radius 20 μm and gap 160 nm at 6.64% off, on average the results are off by 4.7%. Figures 22 and 23 illustrate the results.

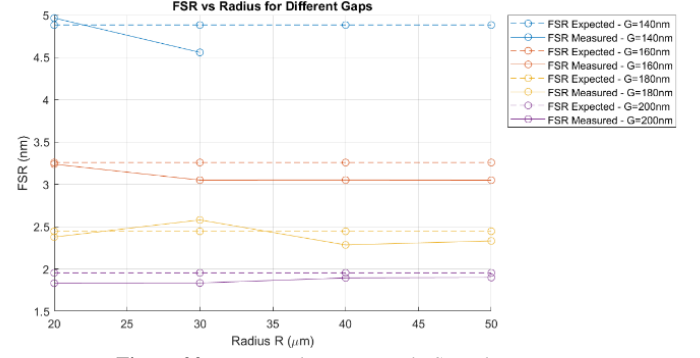


Figure 22 – Expected vs measured FSR values

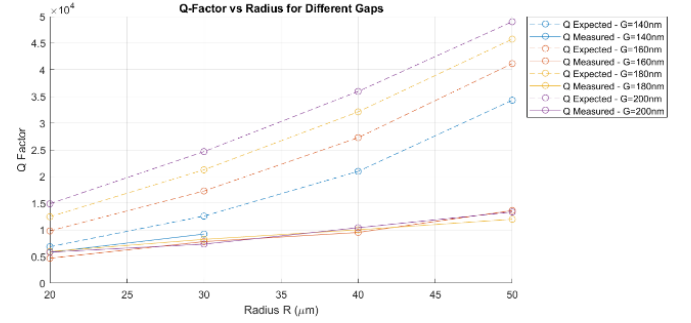


Figure 23 – Expected vs measured Q-factor values

The Q-factor values can be seen following the expected trend, increasing with larger gap sizes and larger ring radii, but are consistently lower than expected values. This may be attributed to the measurement method given the 10 pm resolution. With this resolution, it is likely not possible to detect the true resonance depth at these peak values and therefore calculating the Q-factor from the experimental data proves difficult.

VII. CONCLUSION

To conclude, the designed and simulated MZIs and optical ring resonators closely match with the experimental data of the fabricated devices. The balanced interferometers used for run-run variance, manufacturing and testing repeatability provided a good degree of confidence in the overall process before proceeding to evaluate the imbalanced MZIs and ring resonators. The imbalanced MZIs performed nearly exactly in line with the simulations and expectations, with the 111.46 μm ΔL variant's FSR differing by only 0.3%, the worst performer of the three. The experimental group index value when checked for the MZI case fell within expectations as well at 4.16 instead of 4.19.

The fourteen tested ring resonators also closely follow the expected trends for both the FSR and Q-factor, despite the FSR results themselves differing by 4.7% on average. The Q-factor proved difficult to measure experimentally given the 10 pm resolution. It is likely that higher-resolution measurements (e.g., 1 pm) would yield more accurate Q-factor estimates, better matching the simulated values.

ACKNOWLEDGMENT

I acknowledge the edX UBCx Phot1x Silicon Photonics

Design, Fabrication and Data Analysis course, which is supported by the Natural Sciences and Engineering Research Council of Canada (NSERC) Silicon Electronic-Photonic Integrated Circuits (SiEPIC) Program. The devices were fabricated by Cameron Horvath at Applied Nanotools, Inc. Omid Esmaeeli performed the measurements at The University of British Columbia. I acknowledge Lumerical Solutions, Inc., Mathworks, and KLayout for the design and simulation software.

I would like to also acknowledge the support of my workplace, Fonex Data Systems Inc., in the funding of this course, and to thank the research & development team for their encouragement and continued support in expanding my knowledge into the field of Silicon Photonics.

REFERENCES

- [1] Wim Bogaerts, Peter De Heyn, Thomas Van Vaerenbergh, Katrien De Vos, Shankar Kumar Selvaraja, Tom Claes, Pieter Dumon, Peter Bienstman, Dries Van Thourhout, and Roel Baets, "Silicon microring resonators", *Laser Photonics Rev.* 6, No. 1, 47–73 (2012)
- [2] Lukas Chrostowski, Michael Hochberg, "Silicon Photonics Design: From Devices to Systems", Cambridge University Press, 2015
- [3] <http://siepic.ubc.ca/probestation>, using Python code developed by Michael Caverley.
- [4] Yun Wang, Xu Wang, Jonas Flueckiger, Han Yun, Wei Shi, Richard Bojko, Nicolas A. F. Jaeger, Lukas Chrostowski, "Focusing sub-wavelength grating couplers with low back reflections for rapid prototyping of silicon photonic circuits", *Optics Express* Vol. 22, Issue 17, pp. 20652-20662 (2014) doi: 10.1364/OE.22.020652
- [5] www.plcconnections.com, PLC Connections, Columbus OH, USA.
- [6] <http://mapleleafphotonics.com>, Maple Leaf Photonics, Seattle WA, USA.